Article:
Jin, H., Farrar, M.D., Ball, J.M. et al. (2023) Alumina nanoparticle interfacial buffer layer for low-bandgap lead-tin perovskite solar cells. Advanced Functional Materials, 33 (35). 2303012. ISSN: 1616-301X

https://doi.org/10.1002/adfm.202303012

ADVANCED FUNCTIONAL MATERIALS
www.afm-journal.de

Alumina Nanoparticle Interfacial Buffer Layer for Low-Bandgap Lead-Tin Perovskite Solar Cells

*Heon Jin, Michael D. Farrar, James M. Ball, Akash Dasgupta, Pietro Caprioglio, Sudarshan Narayanan, Robert D. J. Oliver, Florine M. Rombach, Benjamin W. J. Putland, Michael B. Johnston, and Henry J. Snaith**

Mixed lead-tin (Pb:Sn) halide perovskites are promising absorbers with narrow-bandgaps (1.25–1.4 eV) suitable for high-efficiency all-perovskite tandem solar cells. However, solution processing of optimally thick Pb:Sn perovskite films is notoriously difficult in comparison with their neat-Pb counterparts. This is partly due to the rapid crystallization of Sn-based perovskites, resulting in films that have a high degree of roughness. Rougher films are harder to coat conformally with subsequent layers using solution-based processing techniques leading to contact between the absorber and the top metal electrode in completed devices, resulting in a loss of V_{OC}, fill factor, efficiency, and stability. Herein, this study employs a non-continuous layer of alumina nanoparticles distributed on the surface of rough Pb:Sn perovskite films. Using this approach, the conformality of the subsequent electron-transport layer, which is only tens of nanometres in thickness is improved. The overall maximum-power-point-tracked efficiency improves by 65% and the steady-state V_{OC} improves by 28%. Application of the alumina nanoparticles as an interfacial buffer layer also results in highly reproducible Pb:Sn solar cell devices while simultaneously improving device stability at 65 °C under full spectrum simulated solar irradiance. Aged devices show a six-fold improvement in stability over pristine Pb:Sn devices, increasing their lifetime to 120 h.

1. Introduction

Hybrid organic–inorganic metal halide perovskites, as an emerging class of semiconductors, have shown promise as next-generation materials for photovoltaics (PV).[1–5] One attractive property of perovskite semiconductors is the ability to tune their bandgap from ≈1.25 eV to 3.2 eV through compositional engineering of the ABX_3 unit cell,[6–8] with the lowest bandgap materials composed of mixtures of Pb and Sn on the B-site.[9,10] The ability to absorb in the near-infrared portion of the solar spectrum makes narrow-bandgap perovskites well-suited for integration into all-perovskite tandem devices, when paired with wider bandgap perovskites.[11–19] Additionally, the bandgaps in the 1.25–1.4 eV range are theoretically ideal for achieving the highest efficiency single-junction perovskite solar cells (PSCs) according to the detailed balance limit, which is currently only achievable with tin-containing perovskites.[20,21]

Currently, the highest reported PCE for a mixed lead-tin perovskite single junction device is 23.6%, and published all-perovskite tandem solar cells have reached PCE's of over 27%, with press releases of certified cells reporting up to 29% efficiency.[16,17,22] These highest efficiency Pb:Sn perovskite cells employ methylammonium (MA) as an A-site cation, which seems ubiquitous for achieving high efficiencies.[12–14,16,18,22]

The exciton binding energy, on the order of a few meV at room temperature, for Pb:Sn perovskites is considerably lower than that in lead-based perovskites, which can range from

H. Jin, M. D. Farrar, J. M. Ball, A. Dasgupta, P. Caprioglio, R. D. J. Oliver, F. M. Rombach, B. W. J. Putland, M. B. Johnston, H. J. Snaith
Department of Physics
University of Oxford, Clarendon Laboratory
Oxford OX1 3PU, UK
E-mail: henry.snaith@physics.ox.ac.uk

The ORCID identification number(s) for the author(s) of this article can be found under https://doi.org/10.1002/adfm.202303012

DOI: 10.1002/adfm.202303012

S. Narayanan
Department of Materials
University of Oxford
Oxford OX1 3PH, UK

S. Narayanan
The Faraday Institution Quad One
Harwell Science and Innovation Campus
Didcot OX11 0RA, UK

R. D. J. Oliver
Department of Physics and Astronomy
University of Sheffield
Hicks Building, Hounsfield Road, Sheffield S3 7RH, UK

10 to 30 meV.[23,24] The consequence of this is a much weaker absorption coefficient near the band edge, and a requirement to have a relatively thick Pb:Sn absorber layer in order to absorb sufficient infrared (IR) light.[11–15] Although the reason is currently unknown, the presence of MA enables thicker and smoother Pb:Sn perovskite films to be processed. However, MA is known to be chemically and thermally less stable than formamidinium (FA) when incorporated into metal halide perovskites, therefore it would be favorable to have an MA-free Pb:Sn perovskite device that could also deliver high efficiency.[25–28] It is much more challenging to obtain high efficiency with MA-free Pb:Sn perovskites, with only two reports reporting over 20% efficiency.[29,30]

For reasons that remain unclear, Pb:Sn PSCs operate much more efficiently in the positive(p)-intrinsic(I)-negative(n) (p-i-n) configuration than in the n-i-p configuration. In the p-i-n configuration, PSCs have the electron-transport layer (ETL) processed on top, which has been optimized to be an extremely thin (<30 nm) layer of phenyl-C_{61}-butyric acid methyl ester (PCBM) for solution-processed cells, to negate transport losses, alternatively evaporated C_{60} is employed, which also needs to be extremely thin. Even for the Pb-based perovskites, this necessitates extremely smooth underlying perovskite films in order to avoid pinholes in the PCBM layer and consequently direct contact between the metal electrodes and the perovskite film.[31–34] The direct contact between the top metal electrodes and the top of the perovskite film can lead to a relatively low resistance "shunt pathway" through the device, which can lead to substantial losses in fill factor (FF) and open-circuit voltage (V_{OC}), respectively.[35–38] Furthermore, since the dark conductivity in Pb:Sn perovskites is usually orders of magnitude higher than in neat-Pb perovskites, the shunting issue is expected to be exasperated for these narrow-bandgap cells. In addition, this problem is expected to be more problematic for large-area cells with some degree of roughness, where there is a larger probability of shunts forming over the device area.[32,39,40] Therefore, preventing these shunts will be important for scaling-up.

We have historically struggled with obtaining reproducibility in device performance, and suspect that the very thin top layers, coated upon the rough perovskite underlayer could be the primary issue. Here, we investigate the impact of adding a thin layer of alumina nanoparticles (Al_2O_3-NPs) inserted in between the thick, rough perovskite ($FA_{0.83}Cs_{0.17}Pb_{0.5}Sn_{0.5}I_3$) and the ETL in a p-i-n device structure. Such mesoporous alumina layers have previously been used as "buffer layers" in dye-sensitized and early n-i-p PSCs, to inhibit metal migration from the top-metal contact into the solar cell active layer during aging,[41,42] and alumina nanoparticle layers have also been employed to improve the "wettability" of the perovskite absorber layer coating upon the HTM in PSCs.[43–46] Following the "buffer layer" approach, our initial intention was to employ a meso-porous layer of Al_2O_3-NPs to physically block the direct contact between the rough perovskite layer and the top metal electrode. However, we show that an extremely thin non-continuous alumina nanoparticle layer leads to enhanced conformality of the subsequently coated ETL, leading to increases in V_{OC}, PCE and device stability under continuous illumination.

2. Results and Discussion

We used a common one-step anti-solvent quench solution deposition technique to fabricate films of the MA-free narrow-bandgap perovskite, $FA_{0.83}Cs_{0.17}Pb_{0.5}Sn_{0.5}I_3$ (PV bandgap [$E_{g,PV}$] ≈1.27 eV; Figure S12b, Supporting Information [SI]). The bottom half of our solar cell device stack consists of ITO/poly(3,4-ethylenedioxythiophene) polystyrene sulfonate (PEDOT:PSS)/perovskite, with the subsequent electron-transport layer and metal contact being phenyl-C_{61}-butyric acid methyl ester (PCBM)/bathocuproine (BCP)/Ag. In an attempt to improve the interface between the perovskite and top-contact layers, we solution-deposit an alumina nanoparticle layer by spin-coating from dispersions on top of the fully annealed perovskite films. The equivalent thicknesses of the resulting alumina nanoparticle layers depend upon the dilution-ratio of a stock dispersion (<50 nm particle size [DLS], 20 wt.% in isopropanol). We investigated different volumetric dilution ratios of the stock Al_2O_3 dispersion in order to determine the optimal layer thickness: 1:x in IPA, for x = 4, 10, 15, 20, 30, 40, 50, 75, and 100 (the corresponding samples are termed as Al_2O_3_x). The details of the spin-coating recipe are shown in Section S1 (Supporting Information) of the SI.

In complete PSCs, we found that the optimum dilution for Al_2O_3 dispersions was 1:50, corresponding to an equivalent film thickness of only ≈30 nm. We note that we use the term "equivalent thickness" since these films are porous as well as non-continuous at the lower concentration ranges. In **Figure 1**, we show scanning electron microscopy (SEM) images of complete devices, and atomic force microscopy (AFM) images of perovskite films coated with PCBM, with and without the inclusion of the Al_2O_3 nanoparticle interlayer with the 1:50 dilution. Figure 1a shows the cross-sectional SEM image of control devices that had the following structure: ITO/PEDOT:PSS/$FA_{0.83}Cs_{0.17}Pb_{0.5}Sn_{0.5}I_3$/PCBM/BCP/Ag.

The SEM images reveal that there is significant thickness variation in the PCBM layer coating the top of the perovskite film and indicate regions of very close contact between the top metal contact and the polycrystalline perovskite film. In contrast, the cross-sectional morphology of full devices with the Al_2O_3-NPs interlayer, ITO/PEDOT:PSS/$FA_{0.83}Cs_{0.17}Pb_{0.5}Sn_{0.5}I_3$/$Al_2O_3$/PCBM/BCP/Ag, (Figure 1b) exhibits a relatively uniform layer thickness of PCBM between the perovskite film and top metal electrode, with many fewer points of very close contact. To illustrate that this is typical, we show further SEM cross-sectional images of both control and alumina coated devices in Figures S1 and S3 (Supporting Information). We show top-view AFM images of device stacks up to and including the PCBM layer, without and with the inclusion of the Al_2O_3-NPs interlayer in Figure 1c,d respectively. In the control films, absent of Al_2O_3, there appear to be circular "craters" distributed across the film surface. For the films containing the Al_2O_3-NPs interlayer, the craters are not discernible, however, a distribution of features with tens of nanometer length scale are present. In Figure S2 (Supporting Information), we show top-view SEM images of the perovskite films solely coated with the Al_2O_3-NPs dispersion with a 1:50 dilution. Here we observe a distribution of lower electron density features with

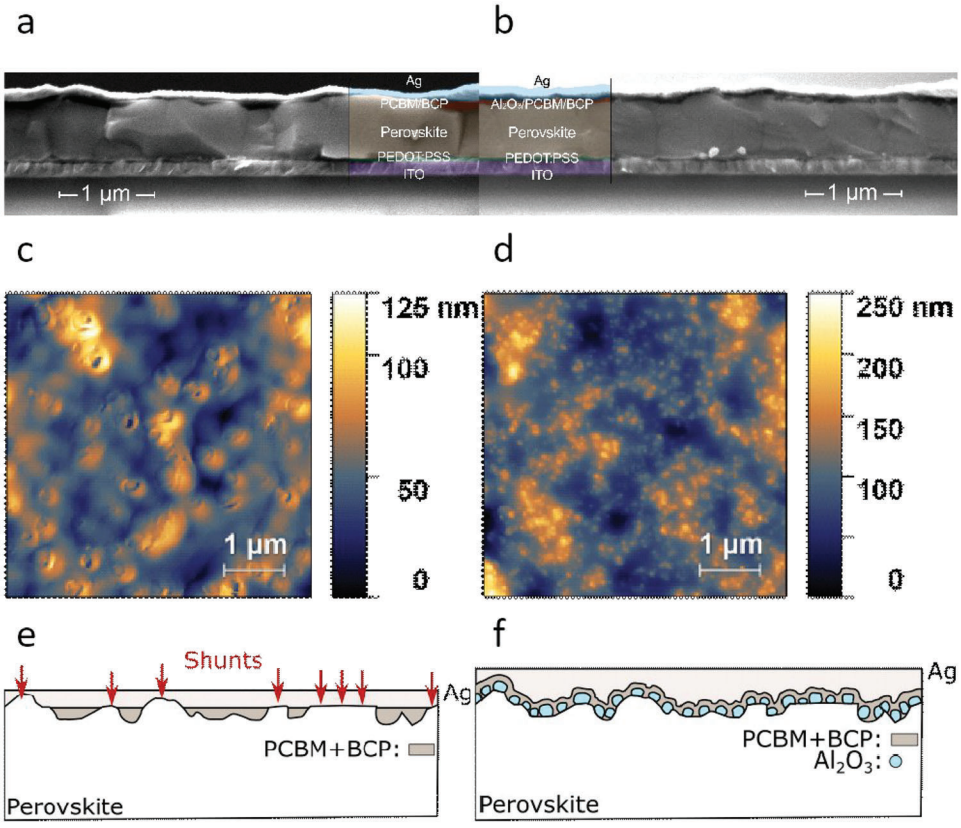

Figure 1. Cross-section SEM images of a) a control device, and b) a device with an Al_2O_3 interlayer. AFM images of c) ITO/PEDOT:PSS/$FA_{0.83}Cs_{0.17}Pb_{0.5}Sn_{0.5}I_3$/PCBM, and d) ITO/PEDOT:PSS/$FA_{0.83}Cs_{0.17}Pb_{0.5}Sn_{0.5}I_3$/$Al_2O_3$/PCBM. Schematic illustrations of how a PCBM layer deposits on a rough mixed Pb:Sn perovskite layer e) without Al_2O_3 f) with Al_2O_3.

tens of nanometer scale distributed in a non-continuous manner over the perovskite film surface. We identify these to be the Al_2O_3-NPs, consistent with the features we observe in the AFM image of Figure 1d.

Furthermore, we performed AFM measurements to examine the surface roughness. First, we compared the root means square (RMS) surface roughness (S_q) of both thin and thick layers of Pb:Sn perovskite films (476.98 and 709.95 nm, respectively, Table S1, Supporting Information) to see how surface roughness varies with perovskite film thickness, noted that thicker narrow-bandgap absorber layers are required for all-perovskite tandem solar cells.[11–15] The RMS surface roughness increases from 27 to 43 nm as the thickness of the perovskite layer increases, which is shown in Figure S4 (Supporting Information).

We also measured the surface roughness of thick perovskite films coated with PCBM using AFM. The perovskite films coated with PCBM (Pero/PCBM) are smoother than the neat perovskite film, with RMS surface roughness reducing from 43 to ≈16 nm. This indicates that the PCBM is "planarizing" the surface, which by itself could be beneficial. However, since the roughness reduction is on the same order of magnitude as the PCBM film thickness, it is likely that very thin regions of PCBM coating exist. In contrast, the perovskite films coated with Al_2O_3 and PCBM (Pero/Al_2O_3/PCBM) show a much smaller reduction in RMS surface roughness from 43 to ≈32 nm, consistent with more conformal coating of the underlying perovskite surface. We show the RMS roughness values in Table S2 (Supporting Information). Figure 1c shows many crater-like shapes on the AFM images. These features are possibly related to bubbles forming during the annealing process of PCBM and may arise from the inhomogeneous thickness of PCBM due to the rough perovskite films. Conversely, when there is an Al_2O_3-NPs layer between the perovskite and the PCBM, the crater-like shapes are no longer observed by AFM (Figure 1d). In Figure 1e, we show a simplified illustration of how PCBM may cover the rough perovskite surface with and without Al_2O_3-NPs.

Encouraged by the improved conformality of the PCBM coating, we investigated the influence of the Al_2O_3-NPs layer on the optoelectronic properties of the perovskite layer and device stack. To do this, we fabricated neat perovskite films and "half-stacks" of perovskite films with hole and electron transport layers, with and without Al_2O_3, and measured their photoluminescence quantum yield (PLQY), time-resolved PL (TRPL) decays, and captured PL images (shown in **Figure 2**; Figures S5–S7). From these results, we can estimate the quasi-Fermi Level splitting (QFLS) in the perovskite absorber layer, which represents the maximum open-circuit voltage the perovskite absorber layer or device stack could generate. The PLQY was measured in an integrated sphere as detailed in Section S1 (Supporting Information) of the SI.

We compared 8 different types of half stack samples: glass/pero (perovskite); glass/pero/Al_2O_3; ITO/HTL (PEDOT:PSS)/pero; ITO/HTL/pero/Al_2O_3; glass/pero/ETL

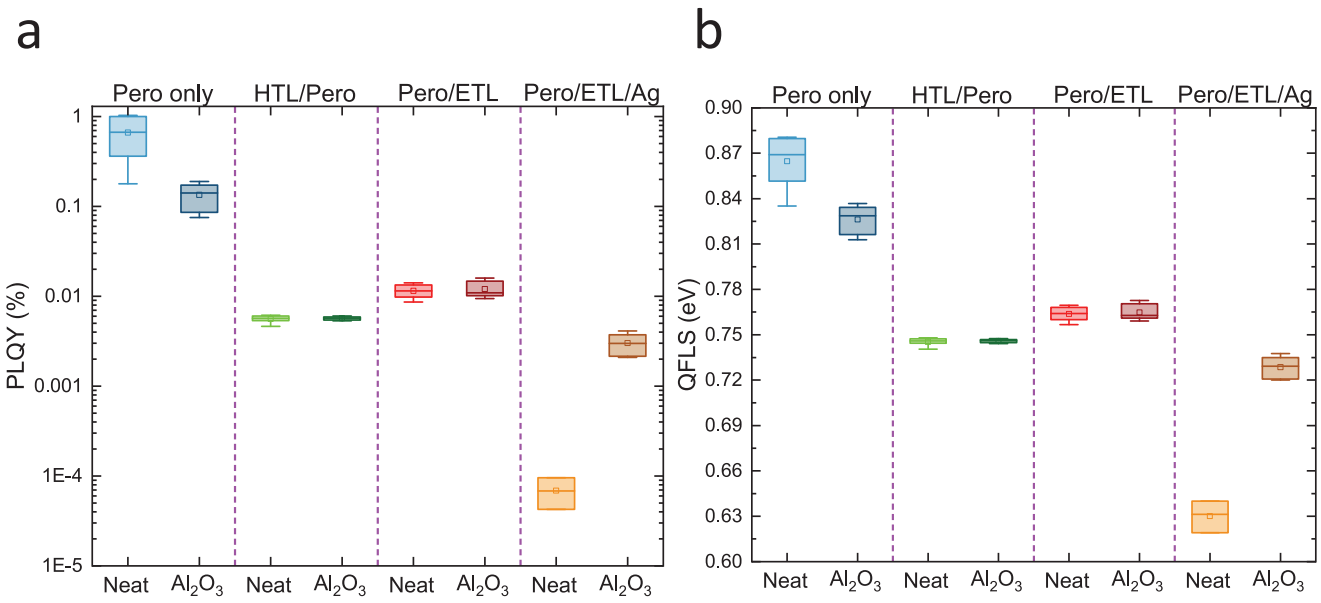

Figure 2. a) PLQY data b) QFLS data from PLQY measurements from 8 different half stack samples with and without Al_2O_3-NPs. Apart from the HTL/pero samples, which are processed on ITO coated glass substrates, all the other samples are processed on glass substrates.

(PCBM/BCP); glass/pero/Al_2O_3/ETL; glass/pero/ETL/Ag; glass/pero/Al_2O_3/ETL/Ag. In Figure 2b, the average QFLS, derived from the PLQY,[47,48] for perovskite films on glass with and without Al_2O_3-NPs layers were 0.86 and 0.83 eV respectively, which indicates that the coating of the perovskite films with the alumina oxide nanoparticles results in a marginal increase in non-radiative recombination at the exposed surface. As previously reported,[49] adding interfaces with charge transport layers can induce a substantial reduction of the PLQY compared to neat perovskite films, indicating recombination losses. The average QFLS for perovskite films with ETL (pero/PCBM/BCP) and films with HTL (PEDOT:PSS/pero) were 0.76 and 0.75 eV, respectively, denoting presence of significant interface recombination in both cases. When combined with Al_2O_3-NPs layers, the QFLS's were also 0.76 and 0.75 eV, respectively for the pero/ETL and HTL/pero stacks, respectively. These findings show that the addition of Al_2O_3 layers does not significantly impact the PLQY of the perovskite layers when integrated into the complete device stacks.[50] Therefore, from the luminescence studies of the isolated perovskite films on glass, and when contacted by the charge extraction layers, we expect to observe a negligible change in V_{OC} for the cells with the inclusion of the alumina particles.

In order to investigate if the presence of metal electrodes introduces further non-radiative recombination, we assessed QFLS data on half-stack samples of the pero/ETL layer with Ag metal back contacts evaporated on top, which we show in Figure 2b. The control samples with metal back contacts (pero/ETL/Ag) exhibited significant reduction in QFLS in comparison with the pero/ETL half-stacks, whereas this additional QFLS loss is largely reduced in the samples containing Al_2O_3-NPs. The significant drop in QFLS following the deposition of the Ag contacts, is likely to arise from some regions of direct contact of the Ag electrode with the perovskite absorber layer. These results are consistent with the presence of the Al_2O_3-NP layer inhibiting direct contact of the metal electrode with the perovskite absorber layer, limiting charge recombination with the metal. In Figures S6 and S7 (Supporting Information), PL imaging was used to quantify macroscopic inhomogeneities on perovskite films on glass with and without Al_2O_3-NPs.[51] We observe that there are some inhomogeneities in the QFLS maps after Al_2O_3-NPs coating. There is a general small reduction in average QFLS on the order of 20 meV, which is similar to what we infer from the macroscopic PLQY results in Figure 2. For the alumina coated samples, there appear to be two distinct regions. As seen in the hysterograms of Figure S6 (Supporting Information), there are some regions that have a similar QFLS distribution to the uncoated perovskite films, and some have lower QFLS. Since we do not know explicitly why the average QFLS is reduced upon alumina coating, it is difficult to postulate as to the origin of this small but observable increase in inhomogeneity. We tentatively interpret this to indicate that the higher QFLS regions are less well-coated with the alumina.

In order to test the functionality of the alumina nanoparticles interlayer in complete devices we fabricated PSCs in a p-i-n architecture: ITO/PEDOT:PSS/$FA_{0.83}Cs_{0.17}Pb_{0.5}Sn_{0.5}I_3$/$Al_2O_3$/PCBM/BCP/Ag, as shown in **Figure 3**a.

We optimized the photovoltaic performance of PSCs based on different dilution ratios of Al_2O_3-NPs to IPA, as shown in Figure 3f and Figure S8 (Supporting Information). For our device parameters, we present the maximum-power-point-tracked efficiency and the steady-state J_{SC} and V_{OC}, the latter two determined by holding the cell at zero volts, and recording the current density over time, or by holding at zero mA cm^{-2} and recording the voltage over time, respectively. The q-FF is an effective FF calculated using, $V_{OC,SS}$, and $J_{SC,SS}$ since a FF cannot be measured in steady-state, as is shown in Equation 1.

$$q-FF = \frac{\eta_{mpp}}{V_{OC,SS} \times J_{SC,SS}} \quad (1)$$

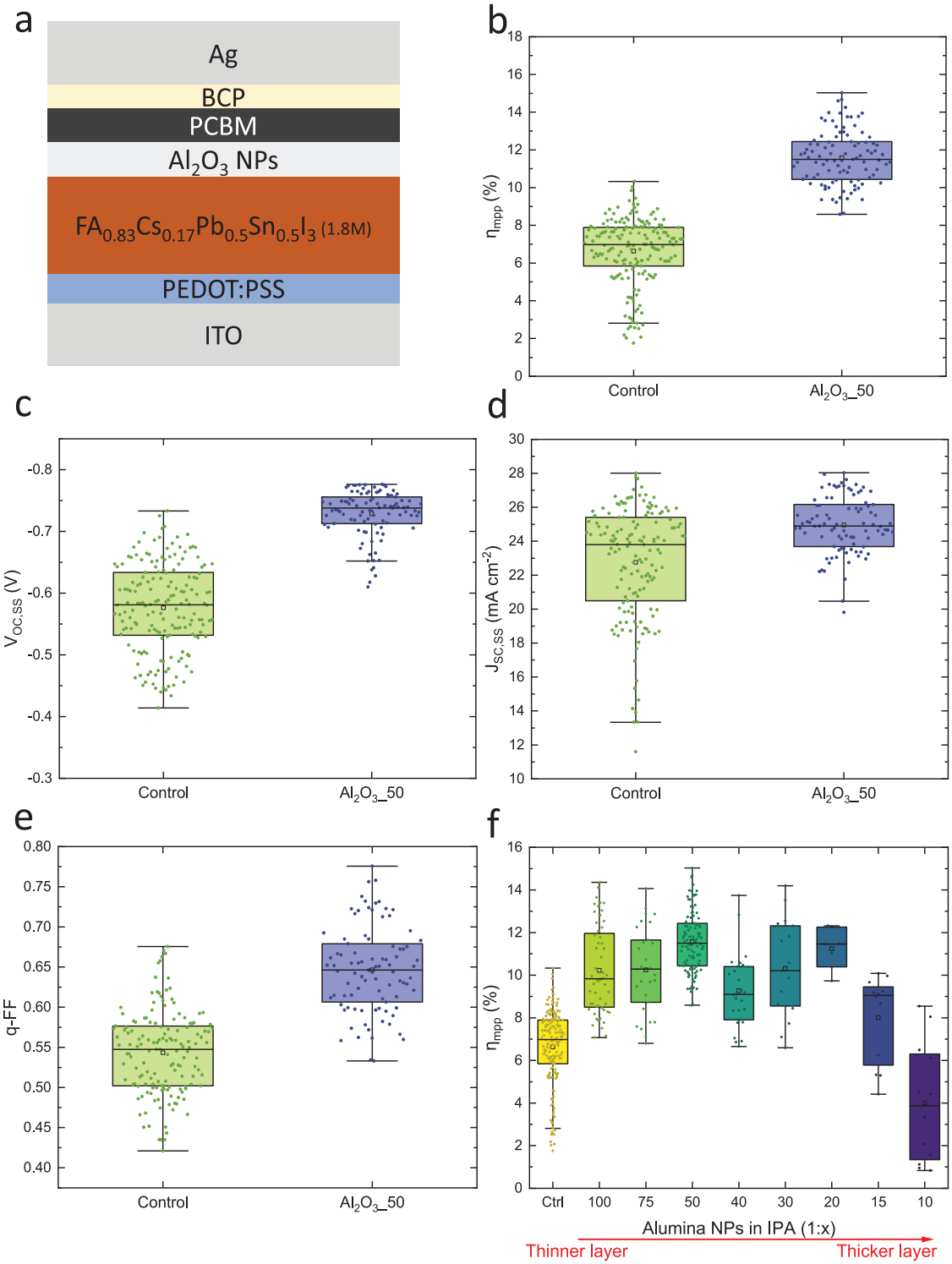

Figure 3. a) Illustration of device structure of Pb:Sn devices coated with an Al_2O_3-NP interlayer. Steady-state (ss) photovoltaic performance parameters: The box plots of b) maximum-power-point-tracked efficiency (η_{mpp}), c) steady-state open-circuit voltage ($V_{OC,SS}$), d) steady-state short-circuit current ($J_{SC,SS}$), e) quasi (q)-FF values for control devices and devices with optimized thickness of alumina nanoparticles. f) η_{mpp} of different dilution ratios of Al_2O_3-NPs to IPA applied on devices.

Table 1. All photovoltaic parameters of devices (derived from steady-state measurements and reverse and forward *J–V* scans) highlighting the champion devices and the median average value of 33 (Al_2O_3-NPs) and 58 (control) identically prepared samples. Each device has 3 pixels with an active area of 0.25 cm^2.

		V_{OC} (V)		J_{SC} (mA cm^{-2})		FF		PCE (%)	
		Best	Average	Best	Average	Best	Average	Best	Average
Al_2O_3-NPs	Steady-state	0.75	0.74	27.95	24.89	0.72	0.65	15.03	11.50
	Reverse	0.75	0.74	28.12	25.51	0.75	0.68	15.92	12.78
	Forward	0.76	0.75	27.99	24.83	0.76	0.67	16.01	12.03
Control	Steady-state	0.65	0.58	25.79	23.80	0.62	0.55	10.33	6.98
	Reverse	0.65	0.60	26.99	24.76	0.62	0.56	10.82	7.81
	Forward	0.66	0.58	26.32	23.84	0.62	0.55	10.80	7.30

Our control devices have significant V_{OC} loss from this limit, with an average steady-state V_{OC} ($V_{OC,SS}$) of 0.58 V. The $V_{OC,SS}$ increases when Al_2O_3-NPs layers are incorporated, with the average $V_{OC,SS}$ equal to ≈0.74 V (Figure S8a, Supporting Information). The maximum-power-point-tracked efficiency (η_{mpp}) has a similar trend (Figure 3f). Beyond a certain thickness, the insulating Al_2O_3-NPs layer leads to the reduction of steady-state J_{SC} ($J_{SC,SS}$) and quasi-steady-state fill factor (q-FF) indicating poor charge extraction

In Figure 3b–e, we show box plots comparing the η_{mpp}, $V_{OC,SS}$, $J_{SC,SS}$, and q-FF of devices with and without an optimized thickness alumina nanoparticles layer. In **Table 1**, we report all photovoltaic parameters of champion and average devices with and without Al_2O_3-NPs layer (steady-state, reverse, and forward *J–V* scan). The average η_{mpp} of Al_2O_3_50 devices is almost twice as large as that of the control devices, which mainly results from the contribution of the significant increase in V_{OC} and FF. The average $V_{OC,SS}$ increases remarkably from 0.58 to 0.74 V in optimized PSCs, and the maximum $V_{OC,SS}$ we achieved was 0.78 V. For reference, the detailed balance limit of V_{OC} for solar cells with a bandgap of 1.27 eV is 1.02 V.[20,52] Similarly, the average q-FF of the control devices increased from 0.55 to 0.65 after applying the insulating buffer layer.

For completeness, we verified that the effect was not a consequence of the IPA solvent within which the Al_2O_3-NP was diluted. We do observe a small, but much less significant improvement upon the solar cell performance after a simple IPA rinse, as shown in Figure S9 and Table S3 (Supporting Information).[53] To examine reproducibility, we fabricated several devices in different batches. As seen in the histogram in Figure S10 (Supporting Information) and the distribution of data points in the box plots in Figure 3b–e, the devices with optimized Al_2O_3 layers show better reproducibility, i.e., their parameter distributions are narrower, than those of control devices.

The difference between the QFLS inferred from the PLQY of either the pero/ETL or HTL/pero stacks, with the average V_{OC} of the complete solar cells, is 180 mV for the control devices and only 10 mV for the devices with the optimized alumina nanoparticle interlayers. This difference in open-circuit voltage loss of the complete solar cells is consistent with the change in estimated QFLS when metal electrodes are deposited on top of the pero/ETL half-stacks. This indicates that the imperfect top contact region is indeed the main origin of voltage loss in the control devices, which is overcome by the more conformal coating of PCBM facilitated by the Al_2O_3-NP buffer layer.

Most control devices have a significant degree of hysteresis, which can be seen in the *J–V* curve of champion control device in **Figure 4**a. All else being equal, significant hysteresis is often correlated with lower η_{mpp} compared to devices with low hysteresis.[54] Figure S11a (Supporting Information) shows the maximum-power-point-tracking (MPPT) of a control and a Al_2O_3_50 device. The champion device with the optimized Al_2O_3-NPs buffer layer achieved a PCE of 15.9%, V_{OC} of 0.75 V, J_{SC} of 28.1 mA cm^{-2}, and FF of 0.75 (reverse scan). Its steady-state photovoltaic parameters are η_{mpp} of 15.0%, $V_{OC,SS}$ of 0.75 V, $J_{SC,SS}$ of 28.0 mA cm^{-2} and q-FF of 0.72. Compared to the control device, all parameters are higher. Interestingly, devices fabricated with Al_2O_3-NPs layer display reduced hysteresis under identical test conditions. In the early days of investigating hysteresis in n-i-p perovskite cells, it was observed that cells that had a complete absence of an electron transport layer and consequently had direct contact between the lead-based perovskites and the electron collection metallic contact (fluorine doped tin-oxide) exhibited extremely severe hysteresis.[55] We thus infer here, that the severe hysteresis in the control devices is due to direct contact between the perovskite absorber layer and the metal top electrode.

Figure S12 (Supporting Information) presents the external quantum efficiency (EQE) spectrum and integrated current density of a control device and a device with the optimized thickness of Al_2O_3-NP interlayer. As shown in Figure S12 (Supporting Information), the EQE of the Al_2O_3_50 device is higher than the control device across the whole wavelength range of 350–950 nm. The integrated value of J_{SC} (27.1 mA cm^{-2}) for a device with Al_2O_3-NPs is consistent with the value of $J_{SC,SS}$ obtained from the *J–V* curves (26.1 mA cm^{-2}). For a control device, the integrated value of J_{SC} (25.5 mA cm^{-2}) is consistent with the value of $J_{SC,SS}$ obtained from the *J–V* curves (25.5 mA cm^{-2}). Notably, the champion device from representative batches with Al_2O_3-NPs showed a higher EQE than the controls.

Having demonstrated a clear improvement in the photovoltaic performance of our devices by incorporating alumina buffer layers, we tried to further optimize their efficiency. One method that has been successfully demonstrated for Pb:Sn perovskites uses ethylenediamine (EDA) passivation, which passivates the perovskite surface and decreases the V_{OC} loss.[56] Here we add EDA directly into the Al_2O_3-NP dispersion so both could be processed in one-step. Figure 4b shows additional *J–V* curve data

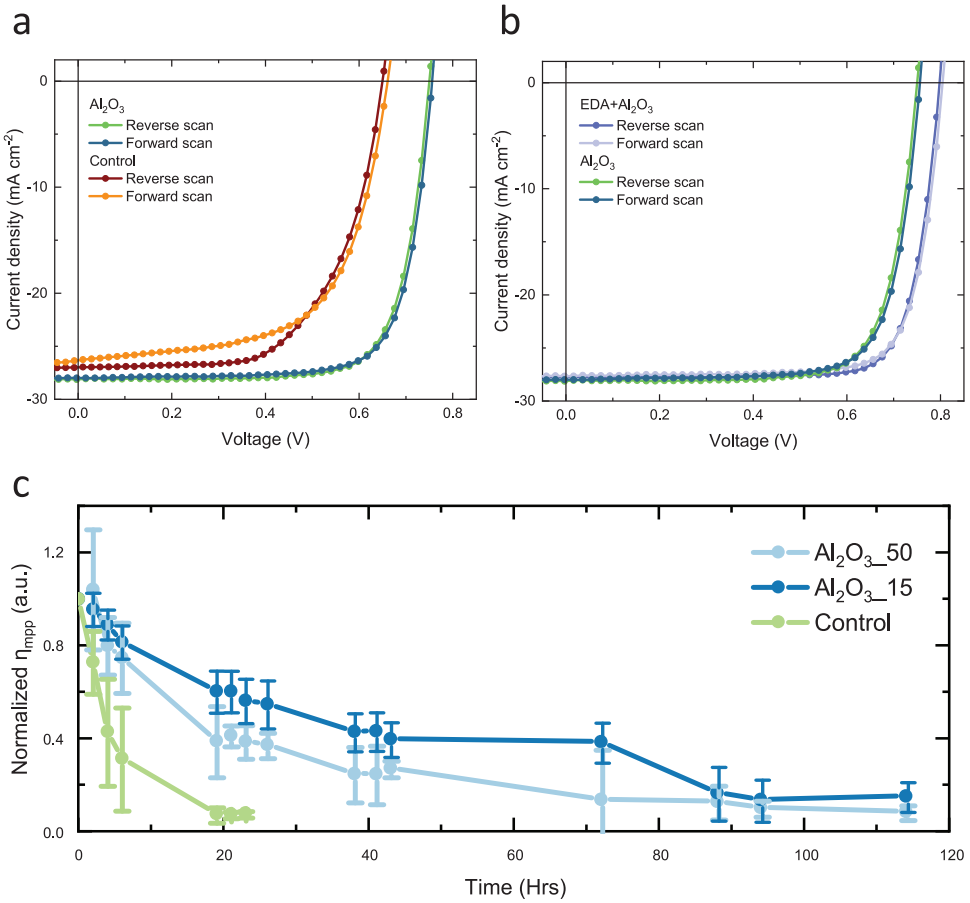

Figure 4. *J–V* curves under simulated AM 1.5G illumination in forward (J_{SC} to V_{OC}) and reverse (V_{OC} to J_{SC}) scan directions of a) the champion control, and the champion device with an optimized Al_2O_3-NP interlayer thickness. b) *J–V* curves of the champion device with optimized Al_2O_3-NP layer thickness, and the champion device with the mixture of EDA and Al_2O_3-NPs. c) Stability assessments of three different encapsulated device configurations under 65 °C, 0.76 Suns AM1.5 irradiance, without UV filter in ambient atmosphere at open-circuit. The initial t = 0, η_{mpp} for the Al_2O_3_50, Al_2O_3_15, and control are 15.37%, 15.12%, and 9.46%, respectively.

of using the mixture of EDA and Al_2O_3-NPs as one interlayer. Similar to applying a neat Al_2O_3-NP layer, the mixture of EDA and Al_2O_3-NPs improved V_{OC} and FF significantly. The improved $V_{OC,SS}$ of the champion device was 0.79 V, and the highest $V_{OC,SS}$ we achieved across all devices in the batch was 0.82 V. The champion device incorporating both EDA and Al_2O_3-NPs had a PCE of 17.5% with a V_{OC} of 0.80 V, J_{SC} of 27.7 mA cm^{-2}, and FF of 0.79 (reverse scan). Its steady-state parameters were η_{mpp} of 16.5%, $V_{OC,SS}$ of 0.79 V, $J_{SC,SS}$ of 27.4 mA cm^{-2}, and q-FF of 0.76 for a device area of 0.25 cm^2 and η_{mpp} of 15.4% at 1.00 cm^2. In comparison, only Werner et al. and Nejand et al. have reported higher PCEs for devices with an area of 1.00 cm^2 in Pb:Sn PSCs.[57,58] All photovoltaic parameters (steady-state, reverse, and forward *J–V* scans) from devices with an area of 1.00 cm^2 are tabulated in Table S5 (Supporting Information). All photovoltaic parameters of devices (steady-state, reverse, and forward *J–V* scans) including average values are shown in Table S4 (Supporting Information). Figure S13 (Supporting Information) shows that applying only the EDA layer for chemical passivation also improves pristine Pb:Sn devices, but the size of the improvement is smaller than using EDA and Al_2O_3-NPs together. The EDA and Al_2O_3-NPs mixture takes on the role of both a chemical passivation and "conformality boosting interlayer". Therefore, using both EDA and Al_2O_3-NPs together synergistically boosts V_{OC}, FF, and PCE.

The long-term stability of PSCs is a key consideration for enabling their real-world use. However, the stability of narrow-bandgap PSCs is limited since mixed Pb:Sn PSCs undergo rapid decay under elevated temperatures and continuous illumination.[25–28,59] To test the impact of the Al_2O_3 interlayer upon the long-term stability under light and elevated temperature, we compared three different types of Pb:Sn PSCs: control devices; devices with optimal thickness of Al_2O_3 layer (Al_2O_3_50); and devices with Al_2O_3 layers as thick as possible that still results in operational cells (Al_2O_3_15). We encapsulated 4 cells for each configuration with epoxy-resin and glass cover-slides, and then subjected them to 0.76 mW cm^{-2} simulated AM1.5 irradiance (generated from a xenon lamp without UV filtering) at 65 °C under open-circuit conditions for 120 h (Figure 4c). We implemented light soaking at 65 °C in an industry-standard aging box, and detailed information is shown in Section S1 (Supporting Information) of the SI. In Figure 4c we plot the normalized η_{mpp} as a function of time. It clearly shows that pristine Pb:Sn devices degraded substantially during the first 6 h of stressing,

and the η_{mpp} of the control Pb:Sn devices maintained only 10% of their initial η_{mpp} after 20 h of light soaking. In contrast, devices with Al_2O_3 layer demonstrated a six-fold slower degradation rate over 120 h. Al_2O_3_50 devices retained >50% of their initial η_{mpp} after 20 h of light soaking. These devices showed complete degradation after ≈120 h of light illumination. Moreover, Al_2O_3_15 devices showed improved light illumination stability, in comparison with the Al_2O_3_50 devices, retaining 60% of the initial η_{mpp} after 20 h of continuous light illumination. Both types of devices with Al_2O_3 layer showed a large improvement of light illumination stability at elevated temperature, compared to pristine devices.

We note that it is quite common to employ evaporated C_{60} in place of PCBM in Pb:Sn PSCs, and often also in conjunction with a metal oxide buffer layer, such as SnO_X, between the C_{60} and the metal top contact.[60–62] One may assume that a thermally evaporated C_{60} layer should be able to conformally coat the top of the rough perovskite layer and be an alternative solution to the issue we are addressing here. However, we test our devices in air, and have found that Pb:Sn PSCs with thermally evaporated C_{60} top contacts drop in performance rapidly when tested in air. Investigating the reason for this stark difference between PCBM and C_{60} is beyond the scope of our study here, but it is clearly an important area to address in future studies.

3. Conclusion

In summary, we have shown through careful optimization that the application of an alumina nanoparticle interlayer, directly between the narrow-bandgap Pb:Sn perovskite absorber layer and PCBM ETL layer, dramatically improves the solar cell device performance and reproducibility. We show compelling evidence that the sparse distribution of alumina nanoparticles on the perovskite surface result in improved conformality of the subsequently coated PCBM layer, reducing the occurrence of close contact between the metallic electrodes and the perovskite absorber layer. As a result, devices that employ this layer achieved a champion η_{mpp} of 15.0% versus 10.3% for the control device. With further passivation using a mixture of EDA and Al_2O_3NPs, we achieved η_{mpp} of 16.5% using a 0.25 cm^2 active area, and up to 15.4% with 1.00 cm^2 active area. The performance spread also showed vast improvement with a median efficiency of 11.5% for devices with Al_2O_3-NPs layer versus 7.0% for controls. Device stability under 65 °C, simulated full spectrum solar irradiance at open-circuit are also greatly improved. This study demonstrates the importance of morphology at device interfaces and presents a facile method to improve interface conformality and inhibit non-radiative recombination losses and electronic shunts occurring in perovskite PV cells.

Supporting Information

Supporting Information is available from the Wiley Online Library or from the author.

Acknowledgements

This work was part funded by the EPSRC, UK, under grant number EP/S004947/1, EP/V010840/1, and EP/T025077/1. H.J. acknowledges the support of the sponsorships from Oxford PV and the Rank Prize. A.D. and B.W.J.P. express their gratitude to the Penrose scholarship for very generously funding their studentships. R.D.J.O. is grateful to the Penrose scholarship for funding his studentship and an EPSRC programme grant (EP/T012455/1) for financial support.

Conflict of Interest

H.J.S. is co-founder and CSO of Oxford PV Ltd., a company commercializing perovskite PV technology.

Data Availability Statement

The data that support the findings of this study are available from the corresponding author upon reasonable request.

Keywords

lead-tin, low-bandgap, methylammonium-free, perovskites, shunt management

Received: April 9, 2023
Published online:

[1] A. Kojima, K. Teshima, Y. Shirai, T. Miyasaka, *J. Am. Chem. Soc.* **2009**, *131*, 6050.
[2] NREL, "Best research-cell efficiency chart, https://www.nrel.gov/pv/cell-efficiency.html," (accessed: May 2023).
[3] H. S. Kim, C. R. Lee, J. H. Im, K. B. Lee, T. Moehl, A. Marchioro, S. J. Moon, R. Humphry-Baker, J. H. Yum, J. E. Moser, M. Grätzel, N. G. Park, *Sci. Rep.* **2012**, *2*, 591.
[4] R. Fickler, R. Lapkiewicz, W. N. Plick, M. Krenn, C. Schaeff, S. Ramelow, A. Zeilinger, *Science* **2012**, *338*, 640.
[5] M. M. Lee, J. Teuscher, T. Miyasaka, T. N. Murakami, H. J. Snaith, *Science* **2012**, *338*, 643.
[6] N. Yaghoobi Nia, D. Saranin, A. L. Palma, A. di Carlo, in *Solar Cells and Light Management: Materials, Strategies and Sustainability*, Elsevier, New York **2019**.
[7] D. P. Mcmeekin, G. Sadoughi, W. Rehman, G. E. Eperon, M. Saliba, M. T. Hörantner, A. Haghighirad, N. Sakai, L. Korte, B. Rech, M. B. Johnston, L. M. Herz, H. J. Snaith, *Science* **2016**, *351*, 151.
[8] R. Prasanna, A. Gold-Parker, T. Leijtens, B. Conings, A. Babayigit, H. G. Boyen, M. F. Toney, M. D. McGehee, *J. Am. Chem. Soc.* **2017**, *139*, 11117.
[9] A. Rajagopal, R. J. Stoddard, H. W. Hillhouse, A. K. Y. Jen, *J Mater Chem A Mater* **2019**, *7*, 16285.
[10] F. Hao, C. C. Stoumpos, R. P. H. Chang, M. G. Kanatzidis, *J. Am. Chem. Soc.* **2014**, *136*, 8094.
[11] M. T. Hörantner, T. Leijtens, M. E. Ziffer, G. E. Eperon, M. G. Christoforo, M. D. McGehee, H. J. Snaith, *ACS Energy Lett.* **2017**, *2*, 2506.
[12] Z. Yang, Z. Yu, H. Wei, X. Xiao, Z. Ni, B. Chen, Y. Deng, S. N. Habisreutinger, X. Chen, K. Wang, J. Zhao, P. N. Rudd, J. J. Berry, M. C. Beard, J. Huang, *Nat. Commun.* **2019**, *10*, 4498.
[13] C. Li, Z. Song, C. Chen, C. Xiao, B. Subedi, S. P. Harvey, N. Shrestha, K. K. Subedi, L. Chen, D. Liu, Y. Li, Y. W. Kim, C. sheng Jiang, M. J. Heben, D. Zhao, R. J. Ellingson, N. J. Podraza, M. Al-Jassim, Y. Yan, *Nat. Energy* **2020**, *5*, 768.
[14] J. Tong, Z. Song, D. Hoe Kim, X. Chen, C. Chen, A. F. Palmstrom, P. F. Ndione, M. O. Reese, S. P. Dunfield, O. G. Reid, J. Liu, F. Zhang, S. P.

Harvey, Z. Li, S. T. Christensen, G. Teeter, D. Zhao, M. M. Al-Jassim, M. F. A. M. van Hest, M. C. Beard, S. E. Shaheen, J. J. Berry, Y. Yan, K. Zhu, *Science* **2019**, *364*, 475.
[15] D. Zhao, Y. Yu, C. Wang, W. Liao, N. Shrestha, C. R. Grice, A. J. Cimaroli, L. Guan, R. J. Ellingson, K. Zhu, X. Zhao, R. G. Xiong, Y. Yan, *Nat. Energy* **2017**, *2*, 17018.
[16] R. Lin, J. Xu, M. Wei, Y. Wang, Z. Qin, Z. Liu, J. Wu, K. Xiao, B. Chen, S. M. Park, G. Chen, H. R. Atapattu, K. R. Graham, J. Xu, J. Zhu, L. Li, C. Zhang, E. H. Sargent, H. Tan, *Nature* **2022**, *603*, 73.
[17] P. Wu, J. Wen, Y. Wang, Z. Liu, R. Lin, H. Li, H. Luo, H. Tan, *Adv. Energy Mater.* **2022**, *12*, 2202948.
[18] D. Zhao, C. Chen, C. Wang, M. M. Junda, Z. Song, C. R. Grice, Y. Yu, C. Li, B. Subedi, N. J. Podraza, X. Zhao, G. Fang, R. G. Xiong, K. Zhu, Y. Yan, *Nat. Energy* **2018**, *3*, 1093.
[19] K. Xiao, R. Lin, Q. Han, Y. Hou, Z. Qin, H. T. Nguyen, J. Wen, M. Wei, V. Yeddu, M. I. Saidaminov, Y. Gao, X. Luo, Y. Wang, H. Gao, C. Zhang, J. Xu, J. Zhu, E. H. Sargent, H. Tan, *Nat. Energy* **2020**, *5*, 870.
[20] W. Shockley, H. J. Queisser, *J. Appl. Phys.* **1961**, *32*, 510.
[21] M. T. Klug, R. L. Milot, R. L. Milot, J. B. Patel, T. Green, H. C. Sansom, M. D. Farrar, A. J. Ramadan, S. Martani, Z. Wang, B. Wenger, J. M. Ball, L. Langshaw, A. Petrozza, M. B. Johnston, L. M. Herz, H. J. Snaith, *Energy Environ. Sci.* **2020**, *13*, 1776.
[22] S. Hu, K. Otsuka, R. Murdey, T. Nakamura, M. A. Truong, T. Yamada, T. Handa, K. Matsuda, K. Nakano, A. Sato, K. Marumoto, K. Tajima, Y. Kanemitsu, A. Wakamiya, *Energy Environ. Sci.* **2022**, *15*, 2096.
[23] Z. Yang, A. Rajagopal, A. K.-Y. Jen, *Adv. Mater.* **2017**, *29*, 1704418.
[24] K. P. Bhandari, A. Lamichhane, T. Maenle, E. Bastola, R. J. Ellingson, *2019 IEEE 46th Photovoltaic Specialists Conference (PVSC)*, Chicago, IL, USA **2019**, pp. 0359–0362.
[25] Z. Song, C. Wang, A. B. Phillips, C. R. Grice, D. Zhao, Y. Yu, C. Chen, C. Li, X. Yin, R. J. Ellingson, M. J. Heben, Y. Yan, *Sustainable Energy Fuels* **2018**, *2*, 2460.
[26] F. Lang, O. Shargaieva, V. v. Brus, H. C. Neitzert, J. Rappich, N. H. Nickel, *Adv. Mater.* **2018**, *30*, 1702905.
[27] H. Turren-Cruz, A. Hagfeldt, M. Saliba, *Science* **2018**, *362*, 449.
[28] E. J. Juarez-Perez, L. K. Ono, Y. Qi, *J Mater Chem A Mater* **2019**, *7*, 16912.
[29] Z. Zhang, J. Liang, J. Wang, Y. Zheng, X. Wu, C. Tian, A. Sun, Z. Chen, C. C. Chen, *Nanomicro Lett* **2022**, *14*, 165.
[30] Z. Yu, J. Wang, B. Chen, M. A. Uddin, Z. Ni, G. Yang, J. Huang, *Adv. Mater.* **2022**, *34*, 2205769.
[31] J. Nelson, *The Physics of Solar Cells*, Imperial College Press, London, United Kingdom **2003**.
[32] M. T. Hörantner, P. K. Nayak, S. Mukhopadhyay, K. Wojciechowski, C. Beck, D. McMeekin, B. Kamino, G. E. Eperon, H. J. Snaith, *Adv. Mater. Interfaces* **2016**, *3*, 1500837.
[33] Y. Zheng, J. Kong, D. Huang, W. Shi, L. Mcmillon-Brown, H. E. Katz, J. Yu, A. D. Taylor, *Nanoscale* **2018**, *10*, 11342.
[34] N. Marinova, W. Tress, R. Humphry-Baker, M. I. Dar, V. Bojinov, S. M. Zakeeruddin, M. K. Nazeeruddin, M. Grätzel, *ACS Nano* **2015**, *9*, 4200.
[35] J. Li, F. Yan, P. Yang, Y. Duan, J. Duan, Q. Tang, *Sol. RRL* **2022**, *6*, 2100791.
[36] G. E. Eperon, V. M. Burlakov, P. Docampo, A. Goriely, H. J. Snaith, *Adv. Funct. Mater.* **2014**, *24*, 151.
[37] J. M. Ball, A. Petrozza, *Nat. Energy* **2016**, *1*, 16149.
[38] J. T. W. Wang, Z. Wang, S. Pathak, W. Zhang, D. W. Dequilettes, F. Wisnivesky-Rocca-Rivarola, J. Huang, P. K. Nayak, J. B. Patel, H. A. Mohd Yusof, Y. Vaynzof, R. Zhu, I. Ramirez, J. Zhang, C. Ducati, C. Grovenor, M. B. Johnston, D. S. Ginger, R. J. Nicholas, H. J. Snaith, *Energy Environ. Sci.* **2016**, *9*, 2892.
[39] C. Blaga, G. Christmann, M. Boccard, C. Ballif, S. Nicolay, B. A. Kamino, *Sustainable Energy Fuels* **2021**, *5*, 2036.
[40] L. Cai, L. Liang, J. Wu, B. Ding, L. Gao, B. Fan, *Journal of Semiconductors* **2017**, *38*, 014006.
[41] S. K. Pathak, A. Abate, T. Leijtens, D. J. Hollman, J. Teuscher, L. Pazos, P. Docampo, U. Steiner, H. J. Snaith, *Adv. Energy Mater.* **2014**, *4*, 1301667.
[42] S. Guarnera, A. Abate, W. Zhang, J. M. Foster, G. Richardson, A. Petrozza, H. J. Snaith, *J. Phys. Chem. Lett.* **2015**, *6*, 432.
[43] D. P. McMeekin, P. Holzhey, S. O. Fürer, S. P. Harvey, L. T. Schelhas, J. M. Ball, S. Mahesh, S. Seo, N. Hawkins, J. Lu, M. B. Johnston, J. J. Berry, U. Bach, H. J. Snaith, *Nat. Mater.* **2023**, *22*, 73.
[44] P. Caprioglio, J. A. Smith, R. D. J. Oliver, A. Dasgupta, S. Choudhary, M. D. Farrar, A. J. Ramadan, Y. H. Lin, M. G. Christoforo, J. M. Ball, J. Diekmann, J. Thiesbrummel, K. A. Zaininger, X. Shen, M. B. Johnston, D. Neher, M. Stolterfoht, H. J. Snaith, *Nat. Commun.* **2023**, *14*, 932.
[45] K. Al Kurdi, D. P. McCarthy, D. P. McMeekin, S. O. Furer, M. H. Tremblay, S. Barlow, U. Bach, S. R. Marder, *Mater. Chem. Front.* **2021**, *5*, 450.
[46] W. Peng, K. Mao, F. Cai, H. Meng, Z. Zhu, T. Li, S. Yuan, Z. Xu, X. Feng, J. Xu, M. D. McGehee, J. Xu, **2023**, *379*, 683.
[47] U. Rau, *Phys. Rev. B* **2007**, *76*, 085303.
[48] P. Caprioglio, M. Stolterfoht, C. M. Wolff, T. Unold, B. Rech, S. Albrecht, D. Neher, *Adv. Energy Mater.* **2019**, *9*, 1901631.
[49] M. Stolterfoht, P. Caprioglio, C. M. Wolff, J. A. Márquez, J. Nordmann, S. Zhang, D. Rothhardt, U. Hörmann, Y. Amir, A. Redinger, L. Kegelmann, F. Zu, S. Albrecht, N. Koch, T. Kirchartz, M. Saliba, T. Unold, D. Neher, *Energy Environ. Sci.* **2019**, *12*, 2778.
[50] P. Caprioglio, D. S. Cruz, S. Caicedo-Dávila, F. Zu, A. A. Sutanto, F. Peña-Camargo, L. Kegelmann, D. Meggiolaro, L. Gregori, C. M. Wolff, B. Stiller, L. Perdigón-Toro, H. Köbler, B. Li, E. Gutierrez-Partida, I. Lauermann, A. Abate, N. Koch, F. de Angelis, B. Rech, G. Grancini, D. Abou-Ras, M. K. Nazeeruddin, M. Stolterfoht, S. Albrecht, M. Antonietti, D. Neher, *Energy Environ. Sci.* **2021**, *14*, 4508.
[51] A. Dasgupta, S. Mahesh, P. Caprioglio, Y. H. Lin, K. A. Zaininger, R. D. J. Oliver, P. Holzhey, S. Zhou, M. M. McCarthy, J. A. Smith, M. Frenzel, M. G. Christoforo, J. M. Ball, B. Wenger, H. J. Snaith, *ACS Energy Lett.* **2022**, *7*, 2311.
[52] Y. Kato, H. Fujiwara, in *Hybrid Perovskite Solar Cells*, Wiley, Weinheim **2021**.
[53] J. W. Yoo, J. Jang, U. Kim, Y. Lee, S. G. Ji, E. Noh, S. Hong, M. Choi, S. il Seok, *Joule* **2021**, *5*, 2420.
[54] A. J. Cimaroli, Y. Yu, C. Wang, W. Liao, L. Guan, C. R. Grice, D. Zhao, Y. Yan, *J Mater Chem C Mater* **2017**, *5*, 10152.
[55] Y. Zhang, M. Liu, G. E. Eperon, T. C. Leijtens, D. McMeekin, M. Saliba, W. Zhang, M. de Bastiani, A. Petrozza, L. M. Herz, M. B. Johnston, H. Lin, H. J. Snaith, *Mater. Horiz.* **2015**, *2*, 315.
[56] G. Kapil, T. Bessho, T. Maekawa, A. K. Baranwal, Y. Zhang, M. A. Kamarudin, D. Hirotani, Q. Shen, H. Segawa, S. Hayase, *Adv. Energy Mater.* **2021**, *11*, 2101069.
[57] J. Werner, T. Moot, T. A. Gossett, I. E. Gould, A. F. Palmstrom, E. J. Wolf, C. C. Boyd, M. F. A. M. van Hest, J. M. Luther, J. J. Berry, M. D. McGehee, *ACS Energy Lett.* **2020**, *5*, 1215.
[58] B. Abdollahi Nejand, I. M. Hossain, M. Jakoby, S. Moghadamzadeh, T. Abzieher, S. Gharibzadeh, J. A. Schwenzer, P. Nazari, F. Schackmar, D. Hauschild, L. Weinhardt, U. Lemmer, B. S. Richards, I. A. Howard, U. W. Paetzold, *Adv. Energy Mater.* **2020**, *10*, 1902583.
[59] E. J. Juarez-Perez, L. K. Ono, M. Maeda, Y. Jiang, Z. Hawash, Y. Qi, *J Mater Chem A Mater* **2018**, *6*, 9604.

[60] K. Xiao, Y. H. Lin, M. Zhang, R. D. J. Oliver, X. Wang, Z. Liu, X. Luo, J. Li, D. Lai, H. Luo, R. Lin, J. Xu, Y. Hou, H. J. Snaith, H. Tan, *Science* **2022**, *376*, 762.
[61] B. Abdollahi Nejand, D. B. Ritzer, H. Hu, F. Schackmar, S. Moghadamzadeh, T. Feeney, R. Singh, F. Laufer, R. Schmager, R. Azmi, M. Kaiser, T. Abzieher, S. Gharibzadeh, E. Ahlswede, U. Lemmer, B. S. Richards, U. W. Paetzold, *Nat. Energy* **2022**, *7*, 620.
[62] A. F. Palmstrom, G. E. Eperon, T. Leijtens, R. Prasanna, S. N. Habisreutinger, W. Nemeth, E. A. Gaulding, S. P. Dunfield, M. Reese, S. Nanayakkara, T. Moot, J. Werner, J. Liu, B. To, S. T. Christensen, M. D. McGehee, M. F. A. M. van Hest, J. M. Luther, J. J. Berry, D. T. Moore, *Joule* **2019**, *3*, 2193.